Chemical Engineering Journal 497 (2024) 154984

Contents lists available at ScienceDirect

Chemical Engineering Journal

journal homepage: www.elsevier.com/locate/cej

Microstructural evolution of Fe-25 W powder beds during CO_2-H_2 redox cycling at 800 °C

Samuel Pennell *, David C. Dunand

Department of Materials Science and Engineering, Northwestern University, Evanston, IL 60208, USA

ARTICLE INFO

Keywords:
CO_2 utilization
Porous materials
Sintering
Redox cycling
Fixed powder bed

ABSTRACT

Fixed powder beds of Fe-25 W at% powders show excellent resistance to degradation during CO_2-H_2 redox cycling at 800 °C, releasing CO and H_2O, respectively, with 100 % metal utilization. During cycling up to 165 full redox cycles (~500 h), the reaction kinetics improve with cycle number and a stable, hierarchically-porous microstructure forms that shows neither sintering nor densification. The sintering inhibition provided by W addition to Fe stems from the formation of Fe-W mixed phases: as an intermetallic compound (Fe_2W) in the reduced state and as a ternary oxide ($FeWO_4$) in the oxidized state. In addition to the large channels running between coarse (100 μm) powder agglomerates, each agglomerate in the powder bed shows both microporosity due to sintering inhibition, and submicron porosity due to a chemical vapor transport reduction mechanism that is active when $FeWO_4$ is reduced by H_2 at high temperature. This hierarchical porosity enables fast reactions due to the short diffusion distance to free surfaces, and non-tortuous gas flow through the powder bed. As a result, under high CO_2 flow, the CO_2:CO ratio is sufficiently high to oxidize Fe_3O_4 to Fe_2O_3, improving the CO conversion capability on a per-mole basis.

1. Introduction

The global goal to limit and eventually stop industrial CO_2 emissions requires carbon capture, utilization, and storage technologies to both limit CO_2 emissions from transitional energy technologies (e.g., natural gas turbines), and to support CO_2-producing chemical reactions, such as cement or steel production [1]. Carbon utilization is the process of converting CO_2 into a more valuable product, often CO (via the reverse water gas shift reaction) or other organic molecules [2,3]. In this way, many industrial processes can be rendered carbon neutral, with all CO_2 emissions being upcycled into alternate products such as acetic acid, hydrocarbon fuels, or polymers.

One approach for carbon utilization uses inorganic materials as oxygen carriers in a chemical looping process: CO_2 emissions are routed through a powder bed of oxygen-carrier powder at high temperature, where CO_2 oxidizes the oxygen carrier, producing CO [4]. Once fully oxidized, the oxygen carrier can be reduced with H_2 produced from water electrolysis, liberating steam and resulting in a full redox cycle. Other chemical looping paradigms, such as the use of methane as the reducing gas [5], are also relevant and will be explored in future work. This CO_2/H_2 cycling method with an oxygen carrier is an alternate method of carrying out the reverse water gas shift reaction. Rather than catalyzing the reaction of CO_2 and H_2 directly with a suitable catalyst such as Ni [6,7] or Mo_2C [8], the reaction is split across two separate stages: the CO_2 oxidation of the oxygen carrier, and the H_2 reduction back to the initial metal state. This paradigm allows for flexibility, as the oxidation and reduction reactions do not need to be carried out in the same location, and the oxygen carrier can be transported as a solid. Suitable oxygen carriers should be robust, with fast oxidation and reduction, a wide operating temperature, and a performance that can tolerate impurities and large particle size.

Due to its low cost, reversible redox cycling capability, and non-toxicity, Fe is viewed as an ideal oxygen carrier material. The oxidation of Fe by CO_2 requires relatively high temperatures to be practically useful, i.e., 600 °C and above [2]. The development of Fe as a high temperature chemical looping technology, particularly for the fixed powder bed configuration, has been held back by the fast sintering and densification of iron and iron oxide powder beds at these elevated temperatures, the same mechanism that occurs with H_2O/H_2 cycling [9,10]. This sintering and densification process causes subsequent redox cycles to be much more sluggish due to poor gas access to the densified powder beds, and long diffusion distances across densified regions.

* Corresponding author.
E-mail address: samuelpennell2024@u.northwestern.edu (S. Pennell).

https://doi.org/10.1016/j.cej.2024.154984
Received 17 June 2024; Received in revised form 11 August 2024; Accepted 18 August 2024
Available online 19 August 2024

Much recent research has attempted to prevent the sintering and densification of Fe powder beds at high temperatures. Use of inert additives such as Al_2O_3 and SiO_2 has shown promise as a low-cost mitigation strategy, with the supporting oxides physically preventing sintering between nearby Fe particles [3,11–15]. Of particular relevance to our work is the study of $FeWO_x$ / SiO_2 powders for which good structural stability, selectivity, and yield for partial oxidation of methane were achieved [15]. However, powder beds with inert additives still show sintering and coarsening over long cycle lifetimes, particularly for micron size rather than nano size powders. Fluidized beds also limit the contact and sintering of particles; a recent study showed the excellent O_2-CO chemical looping behavior of Fe_2O_3 - fluidized beds with 5 mol% W additions [16]. Sintering and densification can still pose a challenge after many cycles, however, and there are additional difficulties present to keep the powders fluidized, such as low density requirement and particle attrition, that can drive up operating costs [17]; also, the powder density is much lower than for fixed powder beds.

In our previous work, we showed the excellent characteristics of Fe-25 at.%W (Fe-52 wt.%W) powder beds under H_2O/H_2 redox cycling, a very similar process of high-temperature oxidation and reduction [18]. The Fe-25 W powder bed shows hierarchical porosity: (i) a continuous microporous network that does not densify due to the sintering inhibition of W; (ii) submicron pores within the struts of the network, formed by the chemical vapor transport reduction of $FeWO_4$ [19–21]. This hierarchical porosity was observed both in freeze-cast foams and in fixed powder beds [22]. Additionally, W does not segregate into pure metallic W or WO_2, due to the atomic-scale mixing of W with Fe in both the reduced and oxidized states. The nominal overall redox reaction of this system is shown in Equation (1). In the reduced state at 800 °C, the Fe-25 W alloy consists of an equimolar mixture of α-Fe and λ-Fe_2W, as shown in the binary Fe-W phase diagram in Supplementary Fig. 1. During oxidation by steam (H_2O), the alloy is transformed into a two-phase oxide mixture of $FeWO_4$ and Fe_3O_4 (with FeO as a transient intermediate phase) and H_2 is liberated:

$$Fe + Fe_2W + \frac{20}{3}H_2O \leftrightarrow FeWO_4 + \frac{2}{3}Fe_3O_4 + \frac{20}{3}H_2 \quad (1)$$

Because, at equilibrium, W is always atomically mixed with Fe – either in the intermetallic Fe_2W or the mixed oxide $FeWO_4$ phase – segregation of W is limited. The overall reaction path is shown in the ternary phase diagram 800 °C isothermal section shown in Supplementary Fig. 2.

In this work, we explore the behavior of the Fe-25 W system when oxidized by CO_2, rather than H_2O. While the differences between H_2O and CO_2 as oxidizing gases may alter the performance of a given metallic powder composition, using the high-performance results from H_2O/H_2 cycling provides a microstructural baseline performance against which the CO_2/H_2 cycling can be directly compared.

Under CO_2 oxidation, the nominal redox reaction as:

$$Fe + Fe_2W + \frac{20}{3}CO_2 \leftrightarrow FeWO_4 + \frac{2}{3}Fe_3O_4 + \frac{20}{3}CO \quad (2)$$

A high theoretical CO production of 1.7 mol CO per mol Fe-25 W alloy (or 0.532 kg CO per kg of Fe-25 W alloy) makes this system attractive, even though the high mass fraction of W (52 wt%) strongly increases the density of the alloy as compared to pure Fe.

Here, we show using, using *in situ* x-ray diffraction and thermogravimetry, that the rate of reaction (which is effectively the CO_2 utilization rate) increases with redox cycle number due to the formation and expansion of porosity in the powder. Additionally, we identify, for the first time, a Fe-based alloy where Fe is oxidized to Fe_2O_3 under CO_2, going beyond the current limits for unalloyed Fe which only achieves Fe_3O_4. The combination of high CO_2 utilization, microstructural stability, and redox cycling stability demonstrate that Fe-W powder beds are excellent candidates for future large-scale CO_2 utilization.

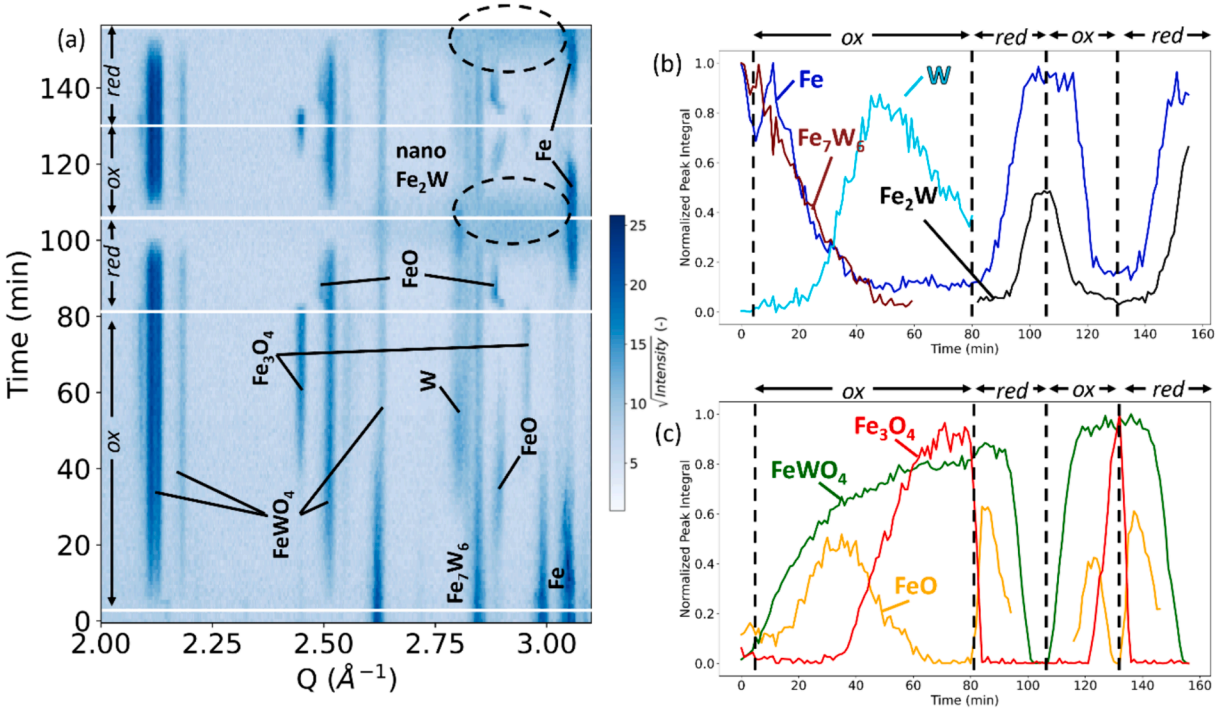

Fig. 1. *In situ* XRD spectra for the first two redox cycles of Fe-25 W powders, performed at 800 °C under flowing CO_2 as oxidizing gas and Ar-4 %H_2 as reducing gas. (a) time-resolved XRD spectra with various phases identified during oxidation (ox) and reduction (red). (b) Normalized peak integrals for metallic phases: Fe (blue), μ-Fe_7W_6 (purple), α-W (cyan) and λ-Fe_2W (black). (c) Normalized peak integrals for oxide phases: FeO (orange), $FeWO_4$ (green), and Fe_3O_4 (red). (For interpretation of the references to colour in this figure legend, the reader is referred to the web version of this article.)

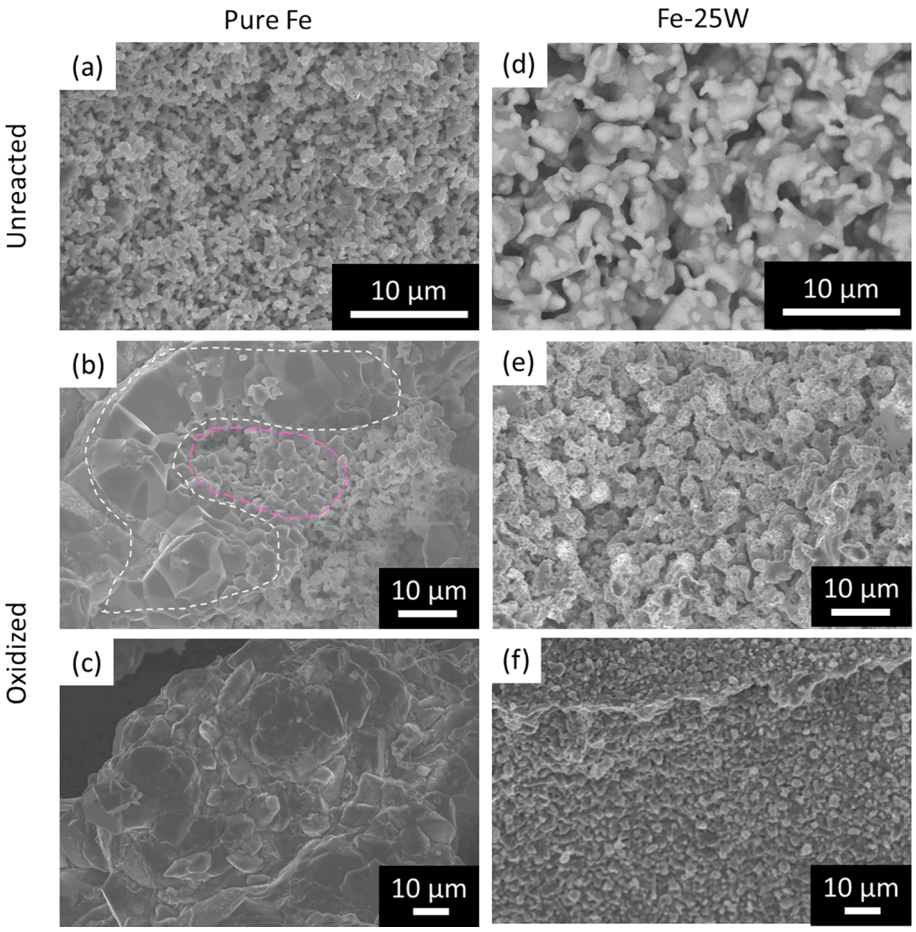

Fig. 2. (a-c) Scanning electron microscopy (SEM) images of the surface of a Fe powder bed (a) before oxidation, (b) after CO_2 oxidation, in a region with both oxide (white dashed region) and metal (pink dashed region). (c) After CO_2 oxidation, in a region with thoroughly sintered oxide surface. (d-f) SEM images of the surface of a Fe-25 W powder bed (d) before oxidation, with a two-phase μ-Fe_7W_6 + α-Fe composition. (e) After CO_2 oxidation in a porous region (f) in a more densified region. Oxidation was performed for 4 h at 800 °C in the TGA instrument.

2. Methods

2.1. Powder bed fabrication

Fe-25 W (at%) powder beds were fabricated from oxide precursors. Slurries were fabricated with Fe_2O_3 (20.4 wt%, Noah technologies, < 3 μm, 99.99 %) and WO_3 (19.7 wt%, US Research Nanomaterials, 100 nm, 99.5 %) powders added to DI water (59.9 wt%) and ball milled on a rotary mill for 24 h to achieve good mixing. Each slurry contained 9.07 g solids. The slurry was dried overnight in a fume hood, then ground into coarse powder agglomerates (approximately 100–300 μm in size) with a mortar and pestle. This coarse powder was poured into an alumina tube (9 mm ID) with quartz wool caps and exposed to flowing H_2, first at 600 °C for 4 h to complete reduction to the metallic state, then at 1200 °C for 3.5 h to achieve partial sintering and give the powder bed sufficient strength to be handled while maintaining porosity throughout the bed. The same procedure was used to fabricate the unalloyed Fe powder beds from the Fe_2O_3 powder, but without the sintering step at 1200 °C, since reduction at 600 °C was sufficient to partially sinter the pure Fe powder beds. Heating and cooling rates of 10 and 5 °C/min, respectively, were used throughout. After sintering, each Fe-25 W powder bed was sectioned with a razor into individual cylindrical bodies with a mass of ~ 1 g each, with 7 mm diameter and 10 mm length.

2.2. Redox cycling

Redox cycling was carried out in an alumina tube furnace (20 mm ID, 500 mm length) at 800 °C (10 °C/min heating rate) under flowing H_2 and CO_2. Alternating reduction and oxidation half-cycles, 90 min each, were achieved by delivery of pure H_2 (UHP, Airgas) and pure CO_2 (Industrial grade, Airgas) using mass flow controller at 200 and 60 sccm, respectively. The gas used during cooldown was either 100 sccm H_2 (for powders in their reduced state) or 20 sccm Ar-4 % H_2 (for powders in their oxidized state). A cooling rate of 5 °C/min was used, and the powder beds were brought to room temperature before removing from the furnace. During cycling, the powders were unconstrained, and thus free to expand and contract during the redox cycles.

2.3. Powder bed microstructural characterization

To obtain cross-sections, powder bed bodies were mounted in epoxy and vacuum-infiltrated to fill porosity before grinding and polishing to 1 μm. Polished samples were sputter-coated with 9 nm Au/Pd for electron microscopy characterization, which was performed with Hitachi SU8030 or Hitachi S4800 instruments on either unmounted powder beds (with as-fabricated surfaces) or mounted and polished powder bed cross-sections.

2.4. X-ray characterization

In-situ X-ray diffraction spectra recorded during redox cycling of powder specimens were collected in a similar setup to our previous work, with minor modifications [23,24]. Spectra were collected on a Stadi-MP (Stoe, Germany) instrument, with an asymmetric curved Ge

monochromator under pure Ag-$K_{\alpha 1}$ radiation (λ = 0.56 Å) and a one-dimensional silicon strip-detector (MYTHEN2 1 k, from Dectris, Switzerland), operated at 40 kV and 40 mA (Beam Size 4 x 0.8 mm). Data were collected in Debye-Scherrer (transmission) geometry, using 1-min scans with 2θ diffraction angles spanning 5.7 to 24.3°, after calibration against a NIST Si standard (640d). A portion of the powder bed was placed in a 1.5 mm diameter quartz capillary and surrounded on both ends by quartz wool. The remainder of the capillary volume on the outlet end of the sample was filled with porous ceramic blocks to prevent sample movement upon changes in gas flow. The capillary was installed into a water-cooled, graphite-heated furnace, with temperature stability of 0.1 °C.

The experiment began by heating the sample to 800 °C (30 °C/min) under 80 sccm flowing Ar-4 % H_2, to ensure the sample remained metallic until the cycling temperature was reached. Once at 800 °C, the gas stream was switched to CO_2 for oxidation, also at 80 sccm. Following complete oxidation, noted by unchanging diffraction patterns, Ar-4 % H_2 was flowed at 80 sccm for reduction. This diluted reduction gas was used to slow the reduction reaction to match the time-resolution of the data collection. A second experiment tested a powder bed sample that had been cycled in the redox station for 10 cycles, then brought to the *in situ* XRD station and tested under the same conditions as above, but at 900 °C. Processing of diffraction patterns was done in Python, with waterfall plots of diffraction spectra, after background correction with a modified polynomial fit. For each phase of interest, the strongest non-overlapping diffraction peak, indexed using reference patterns from the Inorganic Crystal Structure Database (ICSD), was fitted to a Pseudo-Gaussian model using the lmfit package. The peak used for each phase is listed in Supplementary Table 1. These fitted peaks were then integrated to achieve an area, assumed to be proportional to the volume of the diffracting phase, and then normalized to the respective maxima of each phase.

2.5. Thermogravimetry

"Thermogravimetric thermal analyses were performed in a Netzsch STA 449 F3 Jupiter Simultaneous Thermal Analysis (STA) instrument. 20 mg of each powder sample was pre-cycled to the desired cycle number (0, 10, 100, or 165) and was placed in an alumina crucible with weight of 200 mg. Each sample was measured under 30 sccm CO_2 (Research grad, Airgas) with a cover gas of 25 sccm helium (UHP, Airgas). Each sample was ramped and held at 800 °C for 4 h before cooling to room temperature, with heating and cooling rates of 20 and 40 °C/min, respectively.

Buoyancy effect for the gas conditions was corrected by measuring the empty crucible under the same measurement conditions used for the samples Performance of the thermobalance of the STA was verified by using a certified sample of calcium oxalate monohydrate (European Pharmacopoeia Reference Standard) up to 1000 °C. To normalize the data run-to-run, a calibration run with no sample was conducted, and all masses were normalized to the recorded stabilization of gas-flow mass gain (at t = 30 min) from the control run.

3. Results and discussion

3.1. Phase evolution of Fe-25 W powder beds

Fig. 1a shows time-resolved diffraction patterns for the first two CO_2-oxidation/H_2-reduction cycles at 800 °C. Fig. 1b-c shows calculated normalized peak integrals for the strongest peak of each phase, with metallic species shown in Fig. 1b and oxide species shown in Fig. 1c. No carbide phases are observed at any point.

Initially, the powder bed consists of a two-phase mixture of μ-Fe_7W_6 and α-Fe(W), which are the equilibrium phases at the initial sintering temperature of 1200 °C [25], with 1.3 at% W in solid solution within α-Fe(W). When first exposed to CO_2 at 800 °C (at t = 3 min), the powders start to oxidize immediately. Based on the ternary Fe-W-O phase diagram isothermal section at 800 °C (shown in Supplementary Fig. 2), oxidation is expected to occur in three distinct steps: (i) oxidation of λ-Fe_2W to $FeWO_4$ + Fe (ii) oxidation of residual Fe to FeO and (iii) oxidation of FeO to Fe_3O_4. However, since the powder bed initially contained metastable μ-Fe_7W_6 formed at 1200 °C rather than λ-Fe_2W stable at 800 °C, the oxidation pattern of the first oxidation differs from the phase diagram. A transient α-W phase is observed between t = 30 min and t = 80 min, the formation of which is attributed to the sluggish oxidation of W to $FeWO_4$ as compared to the oxidation of Fe to FeO.

The $FeWO_4$ phase is first observed at t = 4 min and takes ~ 60 min to fully form. The formation of $FeWO_4$ occurs in two stages, as shown from the change in slope of the normalized peak integral in Fig. 1c (green). Before t = 18 min, $FeWO_4$ forms relatively quickly, and no other oxide phases are observed. For the next 12 min (t = 18–30 min), transient FeO is observed as expected from the ternary phase diagram, and both $FeWO_4$ and FeO continue to form at approximately the same rate. The FeO peaks show the characteristic shift to higher 2θ as FeO becomes enriched in oxygen [23]. At t = 30 min, several changes occur: FeO begins to be further oxidized to Fe_3O_4, an α-W peak is observed, and the rate of formation of $FeWO_4$ slows to ~ 20 % of the initial rate, as measured by the normalized peak integral. FeO oxidizes to Fe_3O_4 over a 45 min period (t = 18–63 min), and the further oxidation of the α-W into $FeWO_4$ occurs over a 30 min period (t = 50–80 min). Overall, the first CO_2 oxidation half-cycle takes 75 min to complete, and the final state consists of a mixture of $FeWO_4$ and Fe_3O_4, as expected.

The first H_2 reduction half-cycle is comparatively quick, starting at t = 83 min and proceeding ~ 3 times faster than the oxidation step. First, Fe_3O_4 rapidly reduces to transient FeO, over a 2-min period. The FeO peaks show a characteristic shift to lower 2θ as the compounds becomes depleted of oxygen [23]. Then, FeO reduces to Fe over a 10-min period. Reduction of $FeWO_4$ to λ-Fe_2W, the equilibrium intermetallic phase at 800 °C, is the final and slowest step, occurring over a 20-min period. Each of these distinct reduction reactions occurs with an approximately linear rate as measured by the normalized peak integral. This reduction step is expected to occur by the chemical vapor transport reduction mechanism discussed above: $FeWO_4$ is converted to a transient vapor phase $WO_2(OH)_2$, which condenses under flowing H_2 on a freshly-reduced metallic Fe surfaces nearby, where it forms the intermetallic λ-Fe_2W. Because of this reduction mechanism, the λ-Fe_2W formed during cycling is nanocrystalline, as evidenced by broad, low-intensity diffraction peaks [19,22,26,27]. Because of the broad shape of these peaks, the Fe_2W normalized integral signal (black) is low compared to the initial μ-Fe_7W_6 peak or the α-Fe peak, though the amount of W in the system overall is the same.

The second CO_2 oxidation half-cycle, beginning at t = 108 min, is ~ 3.5 times faster than the first due to both the different phase composition (i.e., absence of μ-Fe_7W_6) and the nanocrystalline nature of the λ-Fe_2W present. The same sequence of oxidation is observed, but it occurs over just a 20 min period, rather than the much slower 70 min period of the first oxidation. No transient W peak is observed in the second oxidation, and the normalized peak integral for $FeWO_4$ (Fig. 1b) indicates that the $FeWO_4$ fully and rapidly forms before FeO is observed, as expected from the Fe-W-O ternary phase diagram. Finally, the second H_2 reduction period shows identical rates to the first, again lasting 20-min and following the same sequence, including the formation of nanocrystalline λ-Fe_2W.

3.2. Comparison with pure Fe

The Fe-25 W powder microstructure is compared with the Fe powder microstructure before (Fig. 2a) and after (Fig. 2b-c) oxidation with CO_2 at 800 °C. The unalloyed Fe powder bed (Fig. 2a) is initially highly porous, due to the small size of the original Fe_2O_3 powders and the relatively low reduction temperature. Two regions of the oxidized surface are shown in Fig. 2b-c. Fig. 2b shows a region of incomplete

oxidation, where the growing oxide layer (white dashed region) is growing inwards towards a metallic Fe region (pink dashed region). The oxide grains are much larger than the initial Fe powders, due to both expansion (110 % molar volume expansion) and sintering at high temperatures. In other regions (Fig. 2c) the oxide surface is completely densified, trapping unreacted Fe below the oxide layer and resulting in incomplete reaction. These thoroughly sintered oxide regions contrast starkly with the porous structures observed, even in the oxidized state, for Fe-25 W powders (Fig. 2e-f).

The evolution of Fe-25 W powder beds during oxidation was further explored with TGA under flowing CO_2, shown in Fig. 3, for powder beds either after reduction and sintering (0 cycle), or pre-cycled to 10, 100, and 165 cycles; for comparison, an Fe-only powder was also subjected to TGA after reduction and sintering (0 cycle). A constant flow rate of 30 sccm CO_2 was applied to each sample during a 20 °C/min ramp to 800 °C, followed by a 4 h hold at 800 °C. The expected mass gain for complete conversion of 3Fe to Fe_3O_4 (138 %, brown dashed line) and for complete conversion of Fe-25 W to $Fe_3O_4 + FeWO_4$ (130 %, grey dashed line) are indicated.

The TGA data show that the Fe-25 W powder bed is sluggish to react during the first cycle, reaching only 24 % mass gain in 4 h, compared to an expected maximum mass gain of 30 %. The Fe-25 W powder bed is in fact slower to react than the Fe-only powder bed up to t = 180 min, which reaches 23 % mass gain in the same period, out of an expected maximum mass gain of 38 % for full conversion to Fe_3O_4. The microstructure of the unalloyed Fe powder after CO_2 oxidation in the TGA, shown in Fig. 2, shows the formation of a dense oxide shell, and an initially present microporous network that is completely filled with oxide, slowing further reaction, as expected.

After 10 cycles, however, the Fe-25 W powder bed is much more reactive, rapidly reaching 28 % mass gain in the first 40 min, between t = 40 min (T=575 °C) and t = 80 min (T=800 °C). This is followed by a very slow mass increase to 31 % by t = 240 min. The increase above the expected mass gain is likely due to the formation of Fe_2O_3 in the bed, as confirmed by *ex-situ* XRD.

The mass gain curves for the 100 and 165 cycle specimens are very similar to the 10th cycle one, characterized by a rapid mass gain for t = 40–80 min, followed by a much more gradual mass gain for the remainder of the hold.

Ex situ powder XRD was used to confirm the phases present before and after the TGA experiments. The reduced-state XRD patterns for each specimen are shown in Supplementary Fig. 3a. These reduced-state patterns do not show carbide formation or carbonaceous compounds in the material, indicating that the additional mass gain at 10, 100, and 165 cycles is due to oxide formation not carbon deposition. The oxidized-state patterns shown in Supplementary Fig. 3b, taken after the TGA experiments, indicate the further oxidation of Fe_3O_4 to Fe_2O_3 in the 10-, 100- and 165-cycle powder beds. No carbide phases or carbonaceous compounds are observed in these patterns.

Finally, to assess the formation of Fe_2O_3 under CO_2 oxidation conditions, *in situ* XRD redox cycling was performed on a powder bed that had been pre-cycled to 10 cycles. For this experiment, the cycling temperature was raised to 900 °C to increase the rate of reaction. The results are shown in Fig. 4, with stacked diffraction patterns in Fig. 4a and normalized peak integrals in Fig. 4b-c. Pure CO_2 and H_2 were used as the oxidizing and reducing gases, respectively. The oxidation for the 11th cycle proceeds by the same path and reaction times as seen in cycle 2 in Fig. 1. The initial mixture of λ-Fe_2W and α-Fe(W) first oxidizes to $FeWO_4$, fully forming after 5 min. Transient FeO is formed at the same time, which undergoes a ~1.5 times slower transition to Fe_3O_4 over 7 min, again showing the characteristic peak shifting due to oxygen enrichment. At t = 10 min into the oxidation, as observed in Fig. 4, oxidation would be considered complete and H_2 would be introduced to begin reduction. If CO_2 conditions are held, however, a gradual oxidation of Fe_3O_4 to Fe_2O_3 is observed, occurring over a 40 min period, ~6 times slower than the oxidation of FeO to Fe_3O_4 (t = 20–60 min). The CO_2 oxidative conditions are maintained for another 80 min, but no further changes to the phase composition were observed. The slow rate of oxidation indicates that the formation of Fe_2O_3 observed is indeed due to CO_2, rather than an air leak or other unintended oxygen exposure, which would cause very rapid (<1 min) oxidation to Fe_2O_3.

The formation of Fe_2O_3 is attributed to the highly reactive powder microstructure subjected to a high flow rate of high-purity CO_2. Such conditions, though not usually achieved, can produce Fe_2O_3 under CO_2 conditions so long as the CO_2: CO ratio is very high (<20 ppm CO) [28]. A repeat experiment with lower flow rate (40 sccm) of CO_2 did not show Fe_2O_3 formation, confirming that a high partial pressure of CO_2 is needed for Fe_2O_3 formation.

Subsequent reduction under H_2 (starting at t = 135 min) occurs rapidly, forming first the expected two-phase composition (λ- Fe_2W+α-Fe(W)) after 2 min, which then transforms within 1 min into a mixture of Fe_3W_3C and α-Fe(W). To better clarify the phase evolution in this rapid reduction period, the individual diffraction patterns for the time range t = 136–140 min are shown in Supplementary Fig. 4. Because Fe_2W is observed in only one diffraction pattern, it is omitted from the normalized peak integral calculations. The carbide formation is indicative of the presence of solid C in the powder. This carbon is present due to the Boudouard reaction: $2CO_{(g)} \rightarrow C_{(s)} + CO_{2(g)}$. The occurrence of this

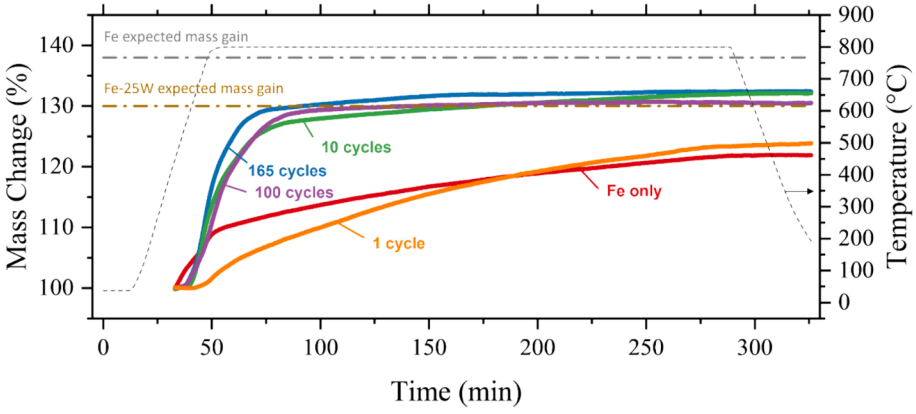

Fig. 3. TGA data (mass gain vs. time) for Fe-25 W specimens subjected to CO_2 oxidation upon heating to, and holding at, 800 °C (temperature profile is shown on the right axis) for their 1st, 10th, 100th, and 165th cycle, for specimens previously subjected to redox cycling outside the TGA. Also shown for comparison is the oxidation for a Fe powder bed for its 1st cycle. The grey and brown dashed line indicate the theoretical mass gain for complete oxidation of Fe (Fe → $\frac{1}{3}$ Fe_3O_4) and Fe-25 W (Fe + Fe_2W→$FeWO_4$ + $\frac{2}{3}$ Fe_3O_4), respectively. The mass change is normalized to the mass reading at t = 32 min; a control run with an empty TGA pan revealed an apparent mass gain (due to gas flow) up to t = 32 min (450 °C): thus, mass gain values measured before this point are inaccurate and are not shown.

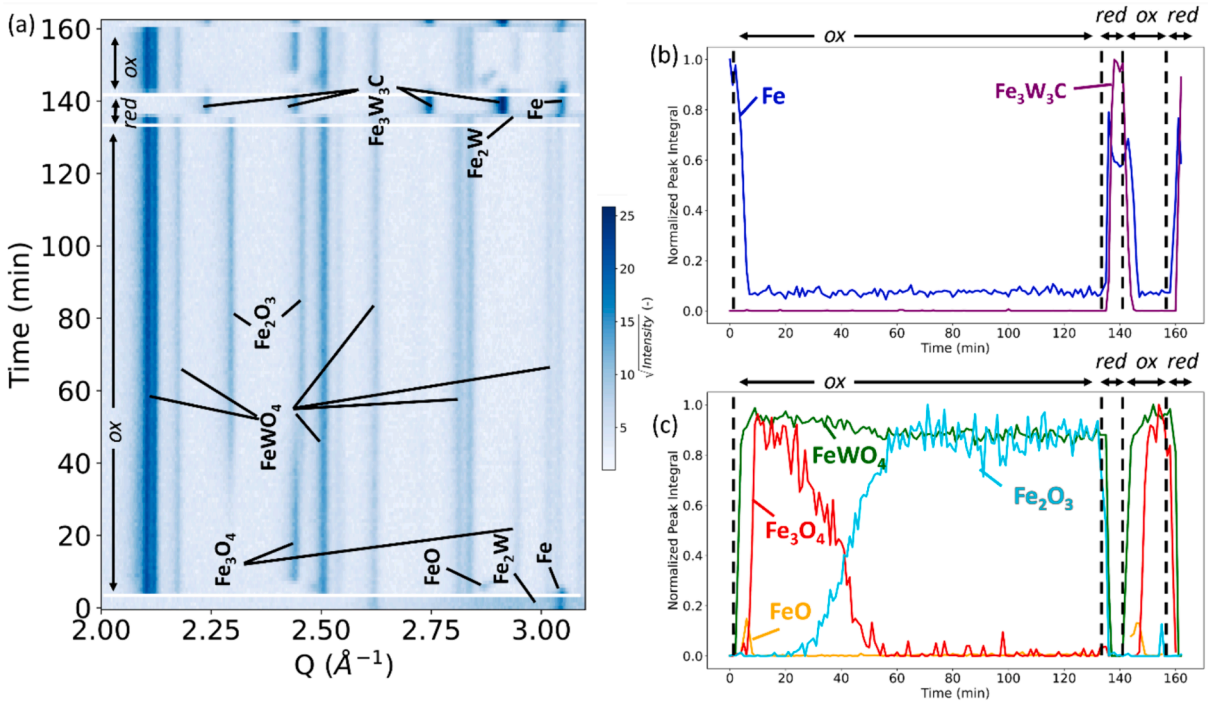

Fig. 4. *In situ* XRD spectra for Fe-25 W starting at cycle 11 at 900 °C, under CO_2 as oxidizing gas and under H_2 as reducing gas. (a) time-resolved XRD spectra showing the phase transformations for 3 half cycles (oxidation–reduction-oxidation). (b) Normalized peak integrals for non-oxide phases: Fe (blue) and λ-Fe_3W_3C (purple). (c) Normalized peak integrals for oxide phases: FeO (orange), $FeWO_4$ (green), Fe_3O_4 (red), and Fe_2O_3 (cyan). (For interpretation of the references to colour in this figure legend, the reader is referred to the web version of this article.)

reaction is attributed to the combination of the reverse water–gas shift reaction ($H_{2(g)} + CO_{2(g)} \rightarrow H_2O_{(g)} + CO_{(g)}$) when H_2 is introduced into the CO_2 environment, combined with the rapid reduction producing metal surfaces onto which C can readily deposit [13]. A repeat experiment with a N_2 flush between oxidizing and reducing conditions did not show carbide formation, indicating that the reverse water–gas shift reaction is responsible for the carbon deposition and carbide formation observed in Fig. 2. These results stress the importance of utilizing a gas-purge step to avoid unintended side reactions during practical operation.

The carbide phase can be re-oxidized, as shown in the second oxidation starting at t = 142 min, and the carbide oxidation occurs at the same rate as metallic oxidation, indicating that the carbide phases do not slow the kinetics of the reaction at a minute-scale temporal resolution. This oxidation releases the CO that was originally disproportionated in the Boudouard reaction. A final reduction at t = 160 min again shows carbide formation. Carbide formation could be suppressed by reacting at higher temperatures, shifting the Boudouard equilibrium to further favor CO, and future work will detail the effect of higher temperature on the reaction process.

3.3. Microstructural evolution

The microstructural evolution of powder beds undergoing CO_2/H_2 cycling is remarkably similar that of H_2O/H_2 cycling [22], since the phases formed are the same in both cases (provided carbide formation is avoided through high flow rate of CO_2). Examples of the porous surface microstructure after 1, 10, 100, and 165 cycles in both the reduced and oxidized states are shown in Fig. 5. After 1 cycle, the reduced state (Fig. 5a) shows a two-phase composition of α-Fe(W) and λ-Fe_2W. The α-Fe(W) regions are 2–5 μm in size (larger regions marked with cyan arrows) and relatively dense, while the λ-Fe_2W regions are <1 μm in size and contain submicron porosity (red arrows). This submicron porosity forms due to the chemical vapor transport reduction mechanism, as explored in Ref. [18]. Throughout the specimen, microscale porosity is prevalent (orange arrows). In the oxidized state (Fig. 5b), however, the volume expansion associated with oxidation results in most pores being closed in the first cycle, leaving a mostly densified oxide surface.

After 10 cycles, the microstructure of the powder bed is quite different, with a foam-like architecture, as shown in Fig. 5c for the reduced state. The large α-Fe(W) regions have shrunk and homogenized, with no clear segregated regions apparent, indicating both phases are in the micron- or submicron size range. Micropores (orange arrows) are more prevalent and they are consistently 1–2 μm in diameter. Submicron pores (red arrows) are seen in all ligaments of the foam, as expected from the nanocrystalline λ-Fe_2W phase formed during H_2 reduction. The 10-cycle oxidized state (Fig. 5d) shows that the micropores are now present even after oxidation (orange arrows). The submicron pores have closed, but the combination of micropores and homogeneously-mixed $FeWO_4$ and Fe_3O_4 prevents sintering or segregation from occurring.

After 100 cycles, the microstructure continues to homogenize and become more foam-like. The ligaments of the foam, shown in the reduced state in Fig. 5e, comprise equiaxed particles with no clear sintering or segregation, and ample microporosity. The small size of the particles makes distinguishing submicron pores more difficult, but the inset (red border) shows nano-scale particles with submicron pores, as expected. The oxidized state (Fig. 5f) remains foam-like, showing similar particle size, and the inset (red border) shows that submicron pores (red arrow) are present in the oxidized state as well, though each phase's size is microcrystalline rather than nanocrystalline. There are no significant changes to the microstructure after 165 cycles, in either the reduced state (Fig. 5g) or the oxidized state (Fig. 5h). In each, micropores and submicron pores are still observed throughout the powder bed.

Fig. 6 shows representative cross sections of the macro-, meso-, and microstructure after 0, 10, 100, and 165 cycles, in the reduced state. The macrostructure of the powder bed changes significantly over 165 cycles, as shown in Fig. 6(a,d,g,j). After the initial sintering step (uncycled), each mm-scale powder bed portion contains a wide distribution of particle agglomerate sizes and porosities, with 20 μm-scale channels (yellow letter C) present between 100 μm-scale powders agglomerates. This structure is also seen after 10 cycles (Fig. 6d), with no significant

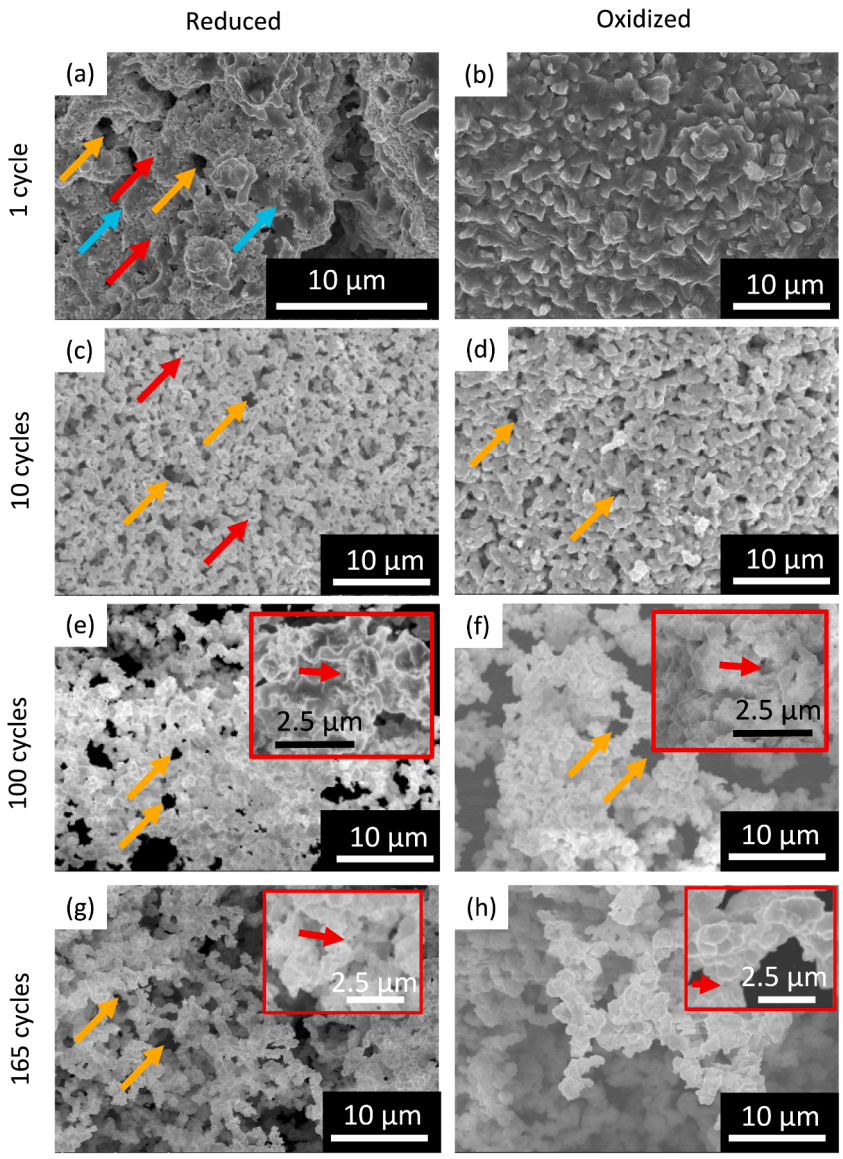

Fig. 5. SEM images showing microstructural evolution of the surface of Fe-25 W powder beds under CO_2/H_2 redox cycling, after (a,b) 1 cycle, (c,d) 10 cycles, (e,f) 100 cycles, and (g,h) 165 cycles, in the (a,c,e,g) reduced and (b,d,f,h) oxidized states. Cyan arrows mark micron-size Fe regions in the first cycle, yellow arrows mark micropores, and red arrows mark submicron pores. Insets in (e-h) show submicron features at higher magnification. (For interpretation of the references to colour in this figure legend, the reader is referred to the web version of this article.)

changes. The wider channels (yellow letter C) between agglomerates seen after 10 cycles is due to the powder bed expanding during mounting in epoxy. After 100 and 165 cycles, sintering of neighboring agglomerates results in the powder bed being much more homogeneous, with no distinct particle agglomerates observed and uniform microporosity throughout.

The overall mesostructure of the powder bed also becomes more porous with cycling, as shown in Fig. 6(b,e,h,k). Initially, each powder agglomerate in the powder bed (Fig. 6b) shows significant (65 %) microporosity due to the sintering inhibition effect of W. The microstructure of the cross section (Fig. 6c) shows ligaments composed of 2–5 µm size regions of α-Fe(W) (blue arrow) and λ-Fe_2W (orange arrow) phases. After 10 cycles (Fig. 6e) the mesostructure is similar to the uncycled state, but the microstructure (Fig. 6f) shows smaller, 1 µm size regions of Fe (blue arrow) and λ-Fe_2W (orange arrow) in the ligaments, with submicron pores present as well. After 100 cycles (Fig. 6h), the porosity of the mesostructure has greatly increased to 80 %, while the microstructure (Fig. 6i) shows submicron phases and a higher volume of submicron pores, with the Fe (blue arrow) and λ-Fe_2W (orange arrow) regions smaller and more difficult to distinguish. After 165 cycles, both mesostructured (Fig. 6k) and microstructure (Fig. 6l) closely resemble those of the 100-cycle powder bed. The overall increase in porosity with cycling is attributed to the cyclic expansion of existing pores by steam released during each reduction half cycle, similar to the formation of pores in the H_2-reduction of iron oxide pellets [29,30], coupled with a near-total inhibition of sintering and densification. These two processes together result in an increase in porosity in the powder bed mesostructure.

4. Conclusions

The microstructural evolution of Fe-25 W powder beds is studied during high temperature CO_2/H_2 redox cycling. After a sluggish first step, the powder beds show accelerating redox kinetics, particularly for oxidation, attributed to the increase in porosity and decrease in phase size that occurs due to the chemical vapor transport reduction of the mixed oxide $FeWO_4$, forming submicron Fe_2W each cycle. The microstructure of the powder beds becomes increasingly porous with cycling

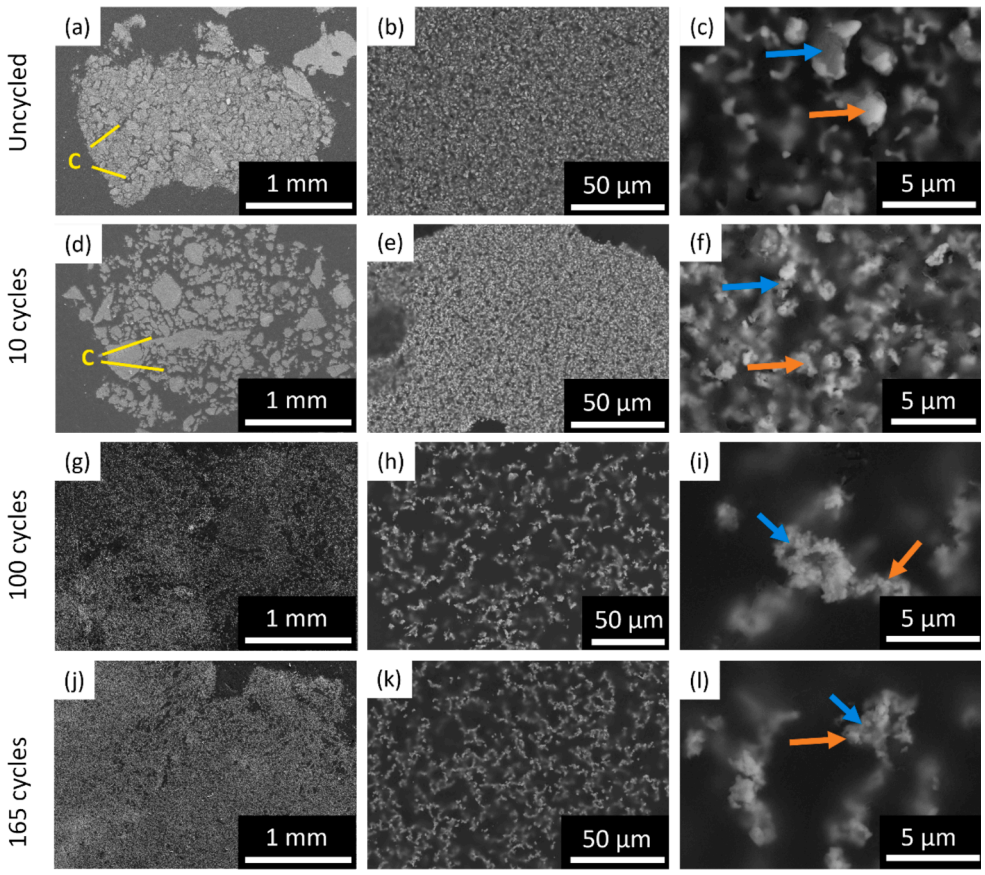

Fig. 6. Cross-sectional SEM images of a Fe-25 W powder bed portion comprising numerous powder agglomerates (100 µm-scale) separated by channels (~50 µm wide, yellow letter C). (a,d,g,j) macrostructure; (b,e,h,k) mesostructure; and (c,f,i,l) microstructure for various cycles: (a,b,c) uncycled, and after (d,e,f)10 cycles, (g,h, i) 100 cycles, and (j,k,l) 165 cycles. Blue arrows mark Fe regions, orange arrows mark Fe_2W regions. (For interpretation of the references to colour in this figure legend, the reader is referred to the web version of this article.)

due to this chemical vapor transport reduction in combination with the excellent sintering inhibition of the intermetallic Fe_2W and the mixed oxide $FeWO_4$. The increasing porosity and decreasing particle size of the powder bed allow for Fe_2O_3 to form under sufficiently high CO_2 flow rate at 800 °C, increasing the oxygen capacity of the material. Overall, this study demonstrates that Fe-25 W powder beds are promising candidates for CO_2 utilization, particularly when used for numerous redox cycles.

CRediT authorship contribution statement

Samuel Pennell: Writing – review & editing, Writing – original draft, Visualization, Project administration, Methodology, Investigation, Conceptualization. **David C. Dunand:** Writing – review & editing, Project administration, Funding acquisition, Conceptualization.

Declaration of competing interest

The authors declare the following financial interests/personal relationships which may be considered as potential competing interests: David Dunand reports financial support was provided by National Science Foundation. Samuel Pennell has patent pending to Northwestern University. Samuel Pennell has patent pending to Northwestern University. If there are other authors, they declare that they have no known competing financial interests or personal relationships that could have appeared to influence the work reported in this paper.

Data availability

Data will be made available on request.

Acknowledgements

This research was funded by the US National Science Foundation under grant CMMI-2015641. Experiments and characterization made use of the Materials Characterization and Imaging Facility, the NUANCE Center, the Jerome B. Cohen X-Ray Diffraction Facility (supported by SHyNE under NSF ECCS-1542205, MRSEC under NSF DMR-1720139, the International Institute for Nanotechnology, the Keck Foundation, and the State of Illinois), and the IMSERC X-Ray facility (supported by SHyNE under NSF ECCS-2025633) at Northwestern University (NU). The authors acknowledge Dr. Ming Chen for useful discussions and advice.

Author contributions

SMP contributed initial writing, illustration, and editing, all experimental work, and project planning and design. DCD contributed project planning and design, and editing.

Appendix A. Supplementary data

Supplementary data to this article can be found online at https://doi.org/10.1016/j.cej.2024.154984.

References

[1] A. Hasanbeigi, L. Price, E. Lin, Emerging energy-efficiency and CO2 emission-reduction technologies for cement and concrete production: A technical review, Renew. Sustain. Energy Rev. 16 (8) (2012) 6220–6238.

[2] J. Hu, V.V. Galvita, H. Poelman, G.B. Marin, Advanced chemical looping materials for CO2 utilizaation: A review, Materials 11 (7) (2018) 1187.

[3] V. Singh, L.C. Buelens, H. Poelman, G.B. Marin, V.V. Galvita, Chemical looping: a technology platform for upcycling low-grade industrial resources, Discov. Chem. Eng. 3 (1) (2023) 12.

[4] S. Valluri, V. Claremboux, S. Kawatra, Opportunities and challenges in CO2 utilization, J. Environ. Sci. 113 (2022) 322–344.

[5] J. Yuan, C. Lu, Z. Gu, J. Cai, H. Zhao, D. Li, L. Jiang, H. Xu, Z.Q. Li, K. Li, Ni-Co catalyst-assisted carbon cycling for CH4-CO2 reforming, Appl. Catal. B 341 (2024) 123318.

[6] E. Gioria, P. Ingale, F. Pohl, R. Naumann d'Alnoncourt, A. Thomas, F. Rosowski, Boosting the performance of Ni/Al2O3 for the reverse water gas shift reaction through formation of CuNi nanoalloys, Cat. Sci. Technol. 12 (2) (2022) 474–487.

[7] A. Wolf, A. Jess, C. Kern, Syngas production via reverse water-gas shift reaction over a Ni-Al2O3 catalyst: catalyst stability, reaction kinetics, and modeling, Chem. Eng. Technol. 39 (6) (2016) 1040–1048.

[8] M. Ahmadi Khoshooei, X. Wang, G. Vitale, F. Formalik, K.O. Kirlikovali, R.Q. Snurr, P. Pereira-Almao, O.K. Farha, An active, stable cubic molybdenum carbide catalyst for the high-temperature reverse water-gas shift reaction, Science 384 (6695) (2024) 540–546.

[9] T. Mattisson, A. Lyngfelt, P. Cho, The use of iron oxide as an oxygen carrier in chemical-looping combustion of methane with inherent separation of CO2, Fuel 80 (13) (2001) 1953–1962.

[10] C.D. Bohn, J.P. Cleeton, C.R. Müller, S.Y. Chuang, S.A. Scott, J.S. Dennis, Stabilizing Iron Oxide Used in Cycles of Reduction and Oxidation for Hydrogen Production, Energy Fuel 24 (7) (2010) 4025–4033.

[11] L.C. Buelens, A.N.V.R. Dharanipragada, H. Poelman, Z. Zhou, G.B. Marin, V. V. Galvita, Exploring the stability of Fe2O3-MgAl2O4 oxygen storage materials for CO production from CO2, J. CO2 Util. 29 (2019) 36–45.

[12] N.V.R.A. Dharanipragada, L.C. Buelens, H. Poelman, E. De Grave, V.V. Galvita, G. B. Marin, Mg–Fe–Al–O for advanced CO2 to CO conversion: carbon monoxide yield vs. oxygen storage capacity, J. Mater. Chem. A 3 (31) (2015) 16251–16262.

[13] B. Jin, N.V. Srinath, H. Poelman, C. Detavernier, Z. Liang, G.B. Marin, V.V. Galvita, Separate H2 and CO production from CH4-CO2 cycling of Fe-Ni, AIChE J 68 (9) (2022) e17779.

[14] Q. Zafar, T. Mattisson, B. Gevert, Redox investigation of some oxides of transition-state metals Ni, Cu, Fe, and Mn supported on SiO2 and MgAl2O4, Energy Fuel 20 (1) (2006) 34–44.

[15] R. Liu, C. Pei, X. Zhang, S. Chen, H. Li, L. Zeng, R. Mu, J. Gong, Chemical looping partial oxidation over FeWOx/SiO2 catalysts, Chin. J. Catal. 41 (7) (2020) 1140–1151.

[16] J.J. Morales Corona, K. Sedransk Campbell, P.S. Fennell, Enhancement of iron-based oxygen carriers through alloying with tungsten oxide for chemical looping applications including water splitting, Greenhouse Gases Sci. Technol. 13 (4) (2023) 565–574.

[17] J.W. Chew, W.C.Q. LaMarche, R.A. Cocco, 100 years of scaling up fluidized bed and circulating fluidized bed reactors, Powder Technol. 409 (2022) 117813.

[18] S. Pennell, M. Chen, D.C. Dunand, Tungsten strongly inhibits sintering of porous iron during high-temperature redox cycling, Small (2024).

[19] R. Morales, D. Sichen, S. Seetharaman, I. Arvanitidis, Reduction of Fe2MoO4 by hydrogen gas, Metall. Mater. Trans. B 33 (4) (2002) 589–594.

[20] H. Kang, Y.-K. Jeong, S.-T. Oh, Hydrogen reduction behavior and microstructural characteristics of WO3 and WO3-NiO powders, Int. J. Refract Metal Hard Mater. 80 (2019) 69–72.

[21] E. Lassner, W.-D. Schubert, Tungsten: Properties, Chemistry, Technology Of The Element, Alloys, And Chemical Compounds, Springer Science & Business Media, 2012.

[22] S. Pennell, M. Chen, D.C. Dunand, Tungsten strongly inhibits sintering of porous iron during high-temperature redox cycling, Small (2024) 2402174.

[23] J.B. Mack, S.M. Pennell, D.C. Dunand, Microstructural evolution of lamellar Fe-25Ni foams during steam-hydrogen redox cycling, Acta Mater. 237 (2022) 118148.

[24] S.M. Pennell, J.B. Mack, D.C. Dunand, Evolution of lamellar architecture and microstructure during redox cycling of Fe-Co and Fe-Cu foams, J. Alloy. Compd. 918 (2022) 165606.

[25] O. Kubaschewski, Iron—Binary phase diagrams, Springer Science & Business Media, Dusseldorf, 1982.

[26] J.B. Mack, S.M. Pennell, D.C. Dunand, Sintering inhibition enables hierarchical porosity with extreme resistance to degradation during redox cycling of Fe-Mo foams, Acta Mater. 119015 (2023).

[27] S.M. Pennell, D.C. Dunand, Microstructure and Phase Evolution of Fe-20Ni-20W Foams During High-Temperature Redox Cycling, Available at SSRN 4784167.

[28] W. Zhang, J. Zhang, Q. Li, Y. He, B. Tang, M. Li, Z. Zhang, Z. Zou, Thermodynamic Analyses of Iron Oxides Redox Reactions, PRICM2013, pp. 777-789.

[29] D. Spreitzer, J. Schenk, Reduction of iron oxides with hydrogen—A review, Steel Res. Internat. 90 (10) (2019) 1900108.

[30] X. Zhou, Y. Bai, A.A. El-Zoka, S.-H. Kim, Y. Ma, C.H. Liebscher, B. Gault, J. R. Mianroodi, G. Dehm, D. Raabe, Effect of pore formation on redox-driven phase transformation, Phys. Rev. Lett. 130 (16) (2023) 168001.